Vol. 47 (2016) ACTA PHYSICA POLONICA B No 6

HEAVY-ION RESULTS OF THE CMS EXPERIMENT*

Bożena Boimska

on behalf of the CMS Collaboration

National Centre for Nuclear Research
Hoża 69, 00-681 Warszawa, Poland

(Received April 29, 2016)

An overview of selected heavy-ion results of the CMS experiment is presented. Jet quenching, quarkonia suppression and two-particle angular correlation results are discussed. The measurements have been performed for lead–lead, proton–lead and proton–proton data samples recorded for Run 1 of the LHC accelerator. In the correlation analysis, low pile-up proton–proton collisions at an energy of 13 TeV (from Run 2) have been used as well.

DOI:10.5506/APhysPolB.47.1397

1. Introduction

Quantum Chromodynamics (QCD) predicts that at extremely high energy densities and temperatures, nuclear matter undergoes a phase transition to a state of deconfined quarks and gluons. This state is called Quark–Gluon Plasma (QGP) and is studied experimentally by colliding heavy ions at relativistic energies. Heavy-ion collisions at the Large Hadron Collider (LHC) allow to study this QCD matter in unexplored, so far, kinematic domain.

The Compact Muon Solenoid (CMS) experiment at the LHC was originally conceived specifically for studies of proton–proton interactions, but exceptional capabilities of CMS enable also studies of a wide range of heavy-ion physics-related observables. It is a multi-layer detector providing nearly 4π coverage. Main parts of the CMS apparatus are the tracking system, calorimeters and muon system, which are covering a wide pseudorapidity (η) range. The high-precision silicon tracking system is located in the 3.8 T field of the superconducting solenoid. It measures charged particles within

* Presented at the Cracow Epiphany Conference on the Physics in LHC Run 2, Kraków, Poland, January 7–9, 2016.

the pseudorapidity range $|\eta| < 2.5$ and consists of silicon pixel and silicon strip detector modules. The electromagnetic (ECAL) and hadron (HCAL) calorimeters are also located inside the solenoid. The ECAL consists of lead–tungstate crystals, arranged in a quasi-projective geometry and distributed in a barrel region ($|\eta| < 1.5$), and two endcaps that extend up to $|\eta| = 3.0$. The HCAL barrel and endcaps are sampling calorimeters composed of brass and scintillator plates, covering $|\eta| < 3.0$. Iron hadronic forward calorimeters (HF) with quartz fibers extend the calorimeter coverage up to $|\eta| = 5.2$. Muons are measured within $|\eta| < 2.4$ in gas-ionization detectors, which are embedded in the steel return yoke. The subdetectors are complemented by a flexible two-level trigger system. A more detailed description of the CMS detector, together with a definition of the coordinate system used, can be found in Ref. [1].

The heavy-ion program carried out by CMS includes studies of lead–lead (PbPb) collisions as well as analyzes for reference systems, *i.e.* proton–lead (pPb) and proton–proton (pp) collisions. In the case of nuclear collisions, the physics observables are usually analyzed in bins of the collision centrality. Centrality can be specified by giving a percentage of the total inelastic cross section. The number of participating nucleons (N_{part}) and the number of binary nucleon–nucleon collisions (N_{coll}) are used as measures of centrality as well. In order to obtain N_{part} and N_{coll} values, the energy measured in HF calorimeters (or event multiplicity from the silicon tracker) is compared to simulations including the Glauber model calculations [2] and the response of the detectors.

During Run 1 of the LHC accelerator, the CMS experiment has recorded $\sim 160\,\mu\mathrm{b}^{-1}$ of PbPb collisions at a nucleon–nucleon center-of-mass energy $\sqrt{s_{NN}} = 2.76$ TeV, $\sim 5.6\,\mathrm{pb}^{-1}$ of pp reference data at the same center-of-mass energy, and $\sim 35\,\mathrm{nb}^{-1}$ of pPb collisions at $\sqrt{s_{NN}} = 5.02$ TeV. In addition, at the end of 2015 (LHC Run 2), PbPb and pp collisions at 5.02 TeV were collected with total integrated luminosities of $\sim 560\,\mu\mathrm{b}^{-1}$ and $\sim 28\,\mathrm{pb}^{-1}$, respectively. Analyzes described in this paper are based only on the Run 1 data samples. There are also some energy dependence studies presented for pp collisions which include results obtained using special low pile-up pp data at higher energies of 7 TeV (Run 1) and 13 TeV (Run 2).

2. Experimental results

A complete collection of all published and submitted CMS heavy-ion papers, as well as a documentation of all preliminary results, can be found in Ref. [3]. This paper focuses only on some selected results concerning jet quenching, quarkonia production and two-particle angular correlations.

2.1. Jet-quenching effect

One of the signatures for the formation of QGP in high-energy heavy-ion collisions is the jet-quenching effect [4]. It has been predicted that interactions of highly energetic partons with the hot and dense colored matter would lead to the depletion of jet yields at high transverse momenta (p_{T}).

2.1.1. Nuclear modification factors

One of the key observables in studies of jet quenching is the nuclear modification factor

$$R_{AA}(p_{\mathrm{T}}) = \frac{1}{T_{AA}} \frac{\mathrm{d}^2 N^{AA}/\mathrm{d}p_{\mathrm{T}}\mathrm{d}\eta}{\mathrm{d}^2\sigma^{NN}/\mathrm{d}p_{\mathrm{T}}\mathrm{d}\eta}\,. \tag{1}$$

Thus, R_{AA} is the ratio of particle yields in nucleus–nucleus (AA) to nucleon–nucleon (NN) collisions, normalized by $T_{AA} = \langle N_{\mathrm{coll}}\rangle/\sigma_{\mathrm{inel}}^{NN}$. The jet-quenching effect is observed when, at high p_{T}, $R_{AA} < 1$.

The CMS has obtained the nuclear modification factors for various particles as well as jets. The results for PbPb and pPb collisions at $\sqrt{s_{NN}} = 2.76$ TeV and 5.02 TeV, respectively, are shown in Figs. 1 and 2.

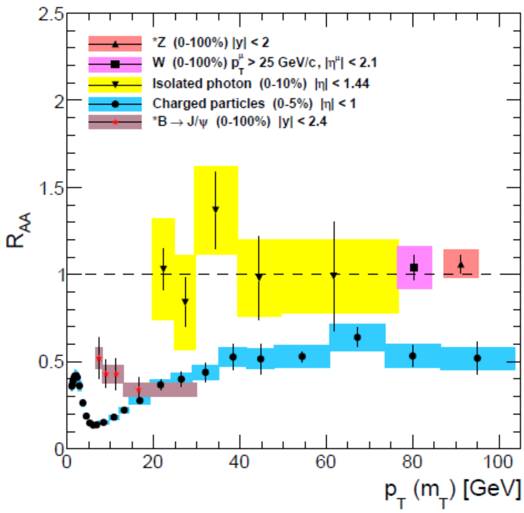

Fig. 1. Nuclear modification factors for isolated photons [5], Z [6] and W [7] bosons, charged hadrons [8] and b-quarks measured by separating secondary J/ψ particles [9]. For Z and W, data points are plotted at the rest mass of particles. For charged hadrons, the pion mass is assumed. Centrality selection for each measurement is indicated in the plot.

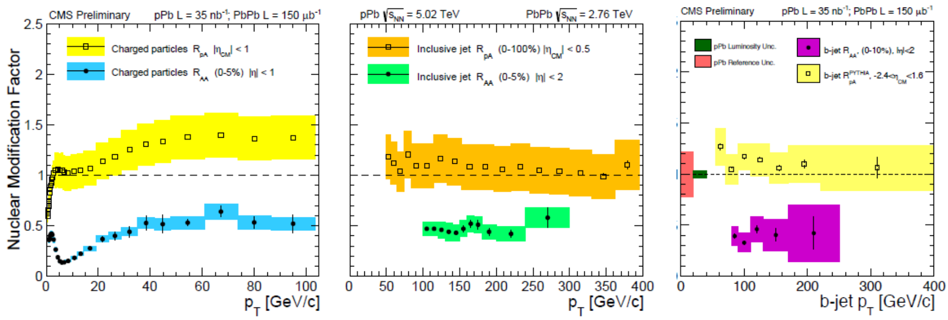

Fig. 2. Nuclear modification factors for central PbPb and centrality-integrated pPb collisions. Left panel: charged particles [8, 10]; Middle panel: inclusive jets [11, 12]; Right panel: jets from b-quarks [13, 14]. Statistical and systematic uncertainties are represented by bars and boxes, respectively. Luminosity uncertainty is indicated by the boxes at b-jet $p_{\mathrm{T}} = 0$.

Bosons mediating electroweak interactions — photon, W and Z — play an important role as reference signals for strongly-interacting probes. In PbPb collisions at $\sqrt{s_{NN}} = 2.76$ TeV, the normalized yield of isolated photons [5] as well as yields of Z [6] and W [7] are consistent with those measured in pp interactions at the same center-of-mass energy, giving $R_{AA} \approx 1$ (see Fig. 1). In contrast to the bosons, for charged hadrons (Fig. 1 or left panel of Fig. 2) and inclusive jets (middle panel of Fig. 2), nuclear modification factors smaller than unity were measured. In central PbPb collisions, the high-p_{T} charged hadrons [8] have $R_{AA} \approx 0.5$, a value very similar to the one found for the inclusive jets [11]. As shown in the right panel of Fig. 2, also the b-jets have the nuclear modification factor $R_{AA} < 1$ [13]. Contrary to the expectations [15], the suppression of b-jets was found to be comparable to that for inclusive jets, at least within present experimental uncertainties. Thus, b-quarks at high transverse momenta seem to suffer a similar amount of energy loss to light quarks and gluons.

In pPb collisions at 5.02 TeV, various manifestations of jet quenching are unseen. The nuclear modification factor of inclusive jets is consistent with unity in centrality-integrated pPb collisions [12], as illustrated by the middle panel of Fig. 2. Within experimental uncertainties, the same observation ($R_{pA} \approx 1$) is made for jets initiated by b-quarks [14] (see the right panel of Fig. 2). For charged particles, an enhancement of the nuclear modification factor at high p_{T} is observed (left panel of Fig. 2). R_{pA} values as large as 1.4 were measured [10] with a systematic uncertainty of 20%. This behavior is currently unexplained; R_{pA} seems to be too large to be explained by an anti-shadowing effect expected in this kinematic region. A significant reduction of the systematic uncertainty can now be achieved using newly collected pp data at the same collision energy of 5.02 TeV.

2.1.2. Study of dijet events

The CMS experiment studied jet quenching by analyzing also dijet events. In the absence of medium effects, the two jets should have transverse momenta of similar magnitude and be emitted back-to-back. In order to characterize the dijet transverse momentum imbalance, an asymmetry ratio was defined as

$$A_{\mathrm{J}} = \frac{p_{\mathrm{T},1} - p_{\mathrm{T},2}}{p_{\mathrm{T},1} + p_{\mathrm{T},2}}\,, \tag{2}$$

where subscripts 1 and 2 refer to the leading and subleading jets in each event, respectively. A_{J} values close to zero imply a balanced dijet configuration, and increasing A_{J} means a stronger suppression of the subleading jet relative to the leading one.

The asymmetry for peripheral and central PbPb collisions at 2.76 TeV is shown in Fig. 3 (top panel) [16]. The A_{J} distribution is in good agreement with the reference distribution (PYTHIA+DATA) for peripheral PbPb colli-

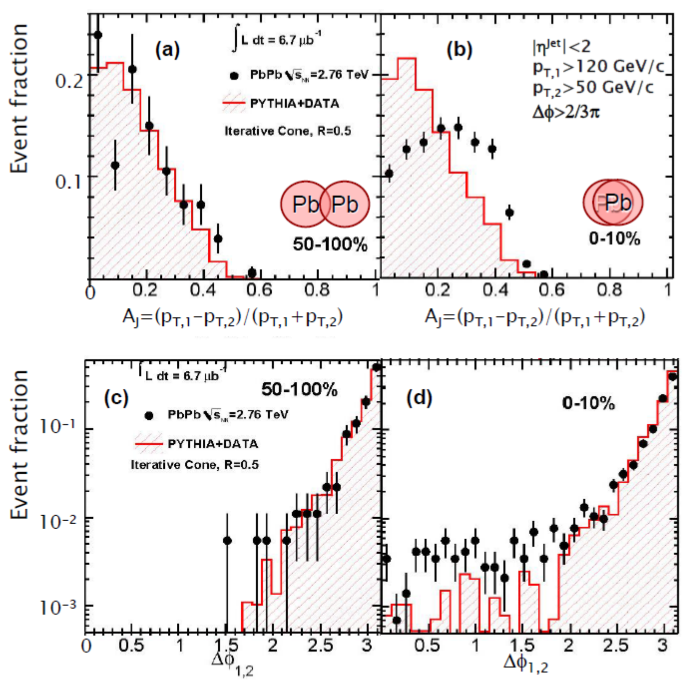

Fig. 3. Top panel: Dijet asymmetry ratio, A_{J}, for leading jets of $p_{\mathrm{T},1} > 120\,\mathrm{GeV}/c$ and subleading jets of $p_{\mathrm{T},2} > 50\,\mathrm{GeV}/c$, separated in azimuthal angle by $\Delta\phi_{1,2} > 2\pi/3$, from 2.76 TeV PbPb data for (a) peripheral 50–100% and (b) central 0–10% collisions. Bottom panel: $\Delta\phi_{1,2}$ distributions for (c) peripheral 50–100% and (d) central 0–10% PbPb collisions. Data are shown as points and PYTHIA dijet events embedded into PbPb data as hatched histograms [16].

sions. The dijet momentum imbalance increases with centrality, and for the (0–10%) most central collisions, the imbalance for PbPb data is significantly larger than that for the reference distribution. This observation is consistent with the scenario in which partons lose their energy traversing the hot and dense QCD medium. On the other hand, the distribution of the azimuthal angle difference between the two jets, $\Delta\phi_{1,2}$, remains sharply peaked at 180 degrees, as shown in Fig. 3 (bottom panel) [16]. This means that the parton energy losses do not cause a strong angular decorrelation of dijets, and rules out single-hard-gluon radiation as the main energy loss mechanism.

The dijet balance has also been studied for pPb collisions at 5.02 TeV. To characterize the dijet transverse momentum imbalance quantitatively, the dijet transverse momentum ratio $p_{\mathrm{T},2}/p_{\mathrm{T},1}$ was used. The $p_{\mathrm{T},2}/p_{\mathrm{T},1}$ ratio was studied as a function of centrality, given by the transverse energy measured in the hadronic forward calorimeters ($E_{\mathrm{T}}^{|\eta|>4}$). In contrast to what is seen in PbPb collisions, no significant dijet transverse momentum imbalance is observed for pPb collisions with respect to the reference data (PYTHIA and PYTHIA+HIJING), as shown in Fig. 4 [17]. Distributions of the dijet azimuthal angle difference $\Delta\phi_{1,2}$ for different centrality classes are sharply peaked at 180 degrees (not shown here), and are in good agreement with the simulated reference distributions [17]. The dijet results from pPb collisions indicate that jet quenching observed in PbPb collisions is a final-state effect.

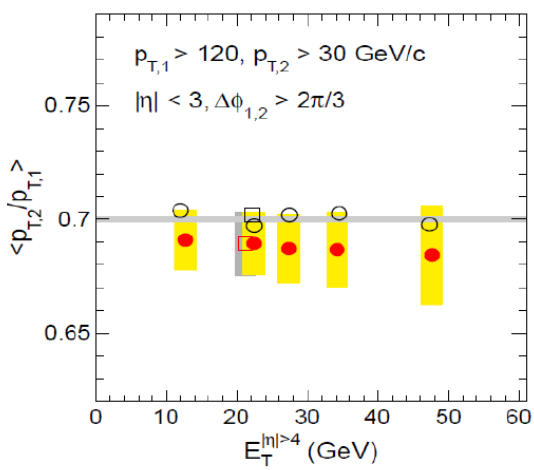

Fig. 4. Average ratio of dijet transverse momenta as a function of $E_{\mathrm{T}}^{|\eta|>4}$ (for leading jets of $p_{\mathrm{T},1} > 120\,\mathrm{GeV}/c$ and subleading jets of $p_{\mathrm{T},2} > 30\,\mathrm{GeV}/c$, separated in azimuthal angle by $\Delta\phi_{1,2} > 2\pi/3$) from 5.02 TeV pPb data (filled circles), compared to the PYTHIA+HIJING (open circles) and PYTHIA (gray band) simulations. The inclusive results for pPb and PYTHIA+HIJING (empty squares) are also shown [17].

2.1.3. Missing transverse momentum

The study of $A_{\rm J}$ for dijet events has shown the presence of $p_{\rm T}$-imbalance of the two jets in central PbPb collisions. In order to find out how the missing transverse momentum is redistributed in phase space, CMS calculated the projection of $p_{\rm T}$ of all reconstructed charged tracks (from the dijet event) onto the leading jet axis

$$\not{p}_{\rm T}^{||} = \sum_{\rm trk} -p_{\rm T}^{\rm trk} \cos\left(\phi_{\rm trk} - \phi_{\rm leading\ jet}\right). \tag{3}$$

The results were then averaged over all events to obtain $\langle \not{p}_{\rm T}^{||} \rangle$. Negative values of $\langle \not{p}_{\rm T}^{||} \rangle$ correspond to the excess towards the leading jet, and positive ones to the excess in the direction of the subleading jet.

The average missing transverse momentum as a function of dijet asymmetry ($A_{\rm J}$), for the 0–30% central PbPb collisions, is shown in Fig. 5. Taking into account all charged particles in the events (left panel), the momentum balance is restored as $\langle \not{p}_{\rm T}^{||} \rangle = 0$ (shown as points). The momentum balance as a function of the distance of tracks from the jet axis, ΔR, was investigated as well[1]. Particles inside jet cones of the size of $\Delta R = 0.8$ around the leading and subleading jet axes (middle panel) and particles outside of these cones (right panel) were used in the study. The in-cone excess towards the leading jet is balanced by the out-of-cone excess in the direction of the sub-

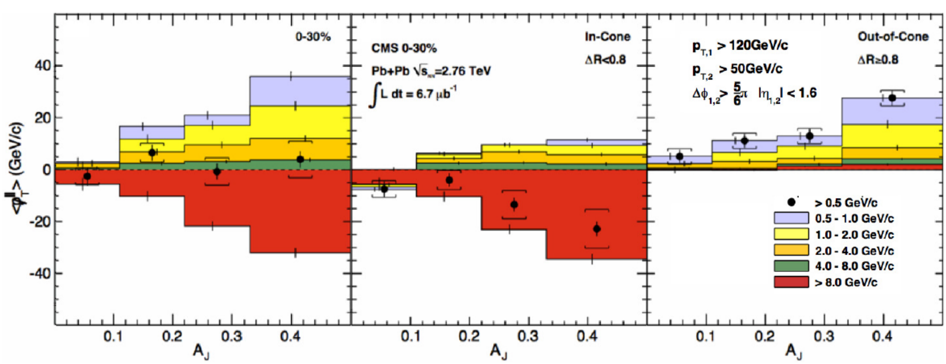

Fig. 5. (Color online) Average missing transverse momentum for the 0–30% central PbPb collisions [16]. Tracks with $p_{\rm T} > 0.5$ GeV/c and $|\eta| < 2.4$ were used. Colored bands show the contributions from various ranges of track $p_{\rm T}$. Points are obtained after summing up all contributions. Left panel: $\langle \not{p}_{\rm T}^{||} \rangle$ for all tracks. Middle panel: $\langle \not{p}_{\rm T}^{||} \rangle$ for tracks inside ($\Delta R < 0.8$) the leading and subleading jet cones. Right panel: $\langle \not{p}_{\rm T}^{||} \rangle$ for tracks outside ($\Delta R > 0.8$) the jet cones.

[1] Jet cone radius $\Delta R = \sqrt{\Delta\eta^2 + \Delta\phi^2}$.

leading jet. The p_{T}-imbalance of the two jets is mainly due to low-p_{T} particles ($p_{\mathrm{T}} < 2\,\mathrm{GeV}/c$) emitted at large angles with respect to the subleading jet axis.

Recently, the angular distribution of $\langle \not{p}_{\mathrm{T}}^{||} \rangle$ for PbPb collisions has been studied more differentially and compared to pp collisions at the same energy [18]. Figure 6 gives an example of these studies, for the inclusive A_{J} selection. The missing transverse momentum $\langle \not{p}_{\mathrm{T}}^{||} \rangle$ as a function of a distance parameter $\Delta = \sqrt{(\eta_{\mathrm{trk}} - \eta_{\mathrm{jet}})^2 + (\phi_{\mathrm{trk}} - \phi_{\mathrm{jet}})^2}$, for reference pp and PbPb in 30–100% and 0–30% centrality binning, is shown across the top panels. In the first bin of Δ, there is a large imbalance towards the leading jet side made up of high-p_{T} tracks, most pronounced in central PbPb collisions. As Δ increases, contributions from softer particles towards the subleading jet side make up this initial imbalance. The imbalance in p_{T}

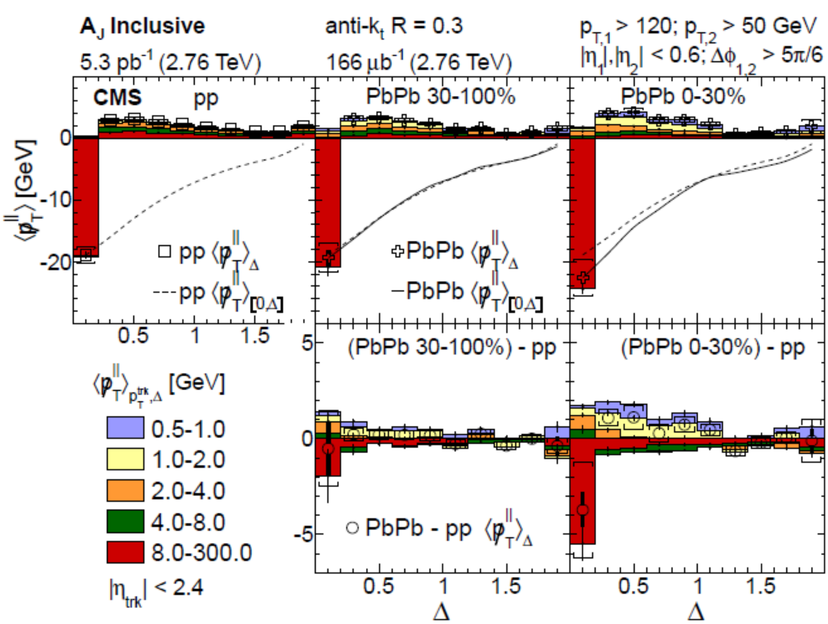

Fig. 6. (Color online) Top row: $\langle \not{p}_{\mathrm{T}}^{||} \rangle$ for pp, 30–100% PbPb, and 0–30% PbPb collisions as a function of Δ. Colored histograms show the contributions for various ranges of track p_{T}. Also shown is $\langle \not{p}_{\mathrm{T}}^{||} \rangle_{\Delta}$ as a function of Δ for pp (open squares) and PbPb data (open plus symbols). Dashed lines (pp) and solid lines (PbPb) show $\langle \not{p}_{\mathrm{T}}^{||} \rangle_{[0,\Delta]}$, *i.e.* $\langle \not{p}_{\mathrm{T}}^{||} \rangle_{\Delta}$ integrated over Δ from $\Delta = 0$ up to the point of interest. Bottom row: Difference between the PbPb and pp $\langle \not{p}_{\mathrm{T}}^{||} \rangle$ distributions according to the range in p_{T}, as a function of Δ (colored histograms), and difference of $\langle \not{p}_{\mathrm{T}}^{||} \rangle_{\Delta}$ as a function of Δ (open circles). Error bars and brackets represent statistical and systematic uncertainties, respectively.

in PbPb collisions is found to be compensated by particles at $p_T = 0.5$–$2\,\mathrm{GeV}/c$, whereas in pp collisions, most of the momentum balance is found in the p_T range of 2–8 GeV/c, reflecting a softening of the radiation responsible for the p_T-imbalance of the asymmetric dijet system in PbPb interactions.

2.1.4. Jet fragmentation functions

The energy loss suffered by the high-p_T partons traversing the medium could modify the fragmentation process. Longitudinal fragmentation is commonly studied as a function of z — a fraction of the parton's momentum carried by a hadron coming from its fragmentation — or as a function of the parameter $\xi = \ln(1/z) = \ln(p^{\text{jet}}/p_{||}^{\text{trk}})$, where p^{jet} is the jet momentum and $p_{||}^{\text{trk}}$ is the projection of track momentum onto the jet axis.

Jet fragmentation functions for different centrality bins of PbPb collisions and pp reference data are shown in Fig. 7 (top row). The bottom panels show ratios of the PbPb and pp fragmentation functions [19]. The peripheral PbPb fragmentation function is in good agreement with that for the pp reference (leftmost panels in Fig. 7). However, for more central collisions, the fragmentation process is modified. In the most central collisions (0–10% centrality bin), there is a strong enhancement of particles at large ξ (corresponding to low p_T), and in the mid-ξ region, a slight depletion is observed.

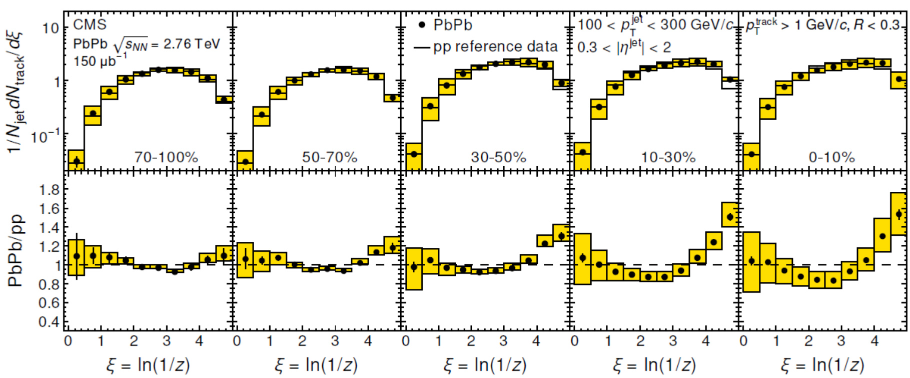

Fig. 7. Top row: Jet fragmentation functions for PbPb collisions (solid points) and for the pp reference (histograms) in five centrality classes; jets with $100 < p_T < 300\,\mathrm{GeV}/c$ and tracks with $p_T > 1\,\mathrm{GeV}/c$, reconstructed within the jet cone of $R = 0.3$, were used. Bottom row: Ratios of each PbPb fragmentation function and the corresponding pp reference. Error bars and boxes represent statistical and systematic uncertainties, respectively.

Results of the jet fragmentation function study for 5.02 TeV pPb collisions are shown in Fig. 8, for the five jet p_{T} bins examined. In order to properly interpret the pPb jet fragmentation function results, a pp reference at the same center-of-mass energy is needed. Unfortunately, no 5.02 TeV pp data had been taken at the time of the analysis, so a pp reference was constructed from the 2.76 and 7 TeV fragmentation functions using a data-driven interpolation technique. The ratio of the pPb fragmentation function and the pp interpolated reference is consistent with unity, indicating that there is no modification of the jet fragmentation function in pPb collisions with respect to the pp interpolated one [20].

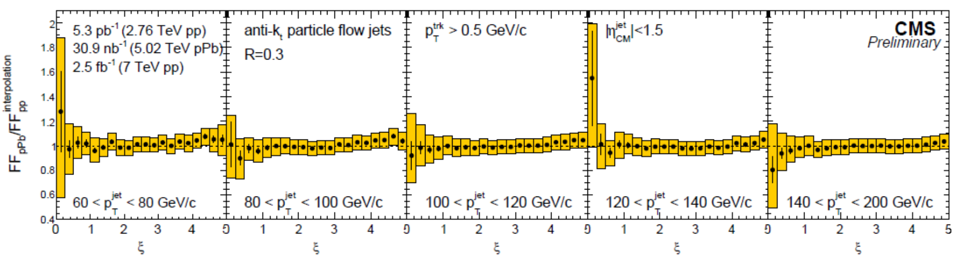

Fig. 8. Ratio of the 5.02 TeV pPb fragmentation function and the pp interpolated reference for different jet p_{T} selections [20]. Underlying event subtraction has been done using a 90 degree rotated cone in the ϕ direction.

The pPb result indicates that the significant modification of the jet fragmentation function seen in central PbPb collisions is due to the creation of the hot dense medium, and not due to cold nuclear matter effects. The interpretation of the pPb result within the context of existing charged particle and jet R_{pA} measurements is more difficult, as these measurements seem to imply a modified pPb fragmentation function which is not seen in this study. One must keep in mind, however, that each of these studies uses a different technique to construct the pp reference spectrum used. 5.02 TeV pp reference data, which has been gathered recently during the LHC Run 2, will remove the need for various interpolation procedures and largely reduce systematic uncertainties. Therefore, the reanalyzes should provide a more definitive description of the relationship between high-p_{T} charged particles and the jets which produced them.

2.2. Quarkonia production

The next signature of QGP creation in heavy-ion collisions is the quarkonia suppression [21]. The suppression, which is expected to originate from color screening of the binding potential of quarkonium states from abundant surrounding light quarks and gluons (Debye screening), is considered as one of the most direct evidence for the deconfinement. Due to the color screening, quarkonia should "melt" and become less abundant. Various quarkonium states have different binding energies and radii, therefore, their dissociation temperatures are different [22]. The sequential melting of quarkonium states, depending on their binding energies, is predicted. The states with low binding energies will melt first, and their yields will be the most suppressed.

The excellent resolution of the CMS muon system enabled measurements of charmonium and bottomonium families in the dimuon decay channel. Figure 9 (left panel) shows the invariant mass distribution of $\mu^+\mu^-$ pairs in the Υ mass region for minimum bias PbPb collisions at 2.76 TeV. Also shown is a fit to the mass distribution from pp collisions at the same energy as PbPb. The plot shows a clear separation of the $\Upsilon(nS)$ states achieved by CMS in both pp and PbPb collisions. The sequential suppression of the three $\Upsilon(nS)$ states in the order of their binding energies is plainly visible in the comparison of the pp line shape and the PbPb data. The right panel of Fig. 9 summarizes the CMS suppression measurements as a function of the binding energy for various quarkonia in minimum bias PbPb collisions. The nuclear modification factors R_{AA} are presented to test the sequential melting prediction. The expected decrease of the suppression (*i.e.* increase in R_{AA}) is indeed observed for states with increasing binding energy. Thus, qualitatively, the sequential melting scenario for quarkonia is confirmed. For quantitative statements further studies have to be done, in which the effects of the p_{T}-cuts and feed-down contributions have to be evaluated.

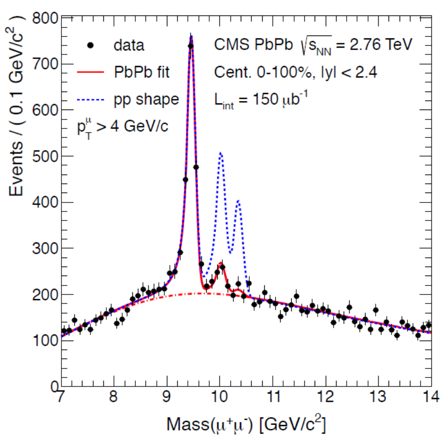

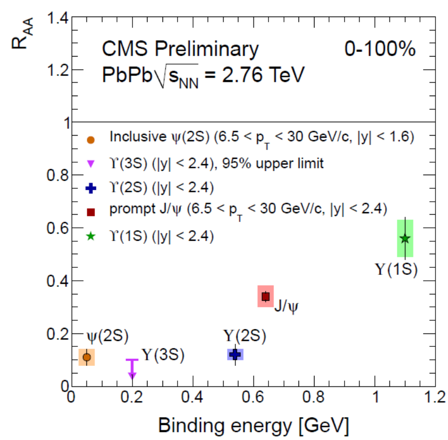

Fig. 9. Left panel: Dimuon invariant-mass distribution in the Υ mass region. The solid line shows the fit to the minimum bias PbPb data at $\sqrt{s_{NN}} = 2.76$ TeV. The dashed line is the fit to the spectrum in pp collisions at 2.76 TeV, normalized to the $\Upsilon(1S)$ peak in PbPb. Right panel: Minimum bias R_{AA} for all quarkonia measured by CMS: high-p_{T} states of prompt J/ψ [9] and inclusive $\psi(2S)$ [23], as well as $\Upsilon(1S, 2S, 3S)$ states [24]. For $\Upsilon(3S)$, the upper limit (95% C.L.) is given.

Recent results, obtained for high statistics PbPb and pp data, on the nuclear modification factor of $\Upsilon(1S)$ and $\Upsilon(2S)$ are shown in Fig. 10. A strong, centrality-dependent suppression is observed in PbPb collisions. The yield is suppressed by up to a factor of 2 and 10 for the $\Upsilon(1S)$ state and the $\Upsilon(2S)$ state, respectively. No pronounced dependence on transverse momentum or rapidity is observed — R_{AA} distributions are constant within uncertainties as a function of both p_{T} and y. The $\Upsilon(3S)$ state was not observed in PbPb collisions, being suppressed by more than a factor of 7 at 95% C.L.

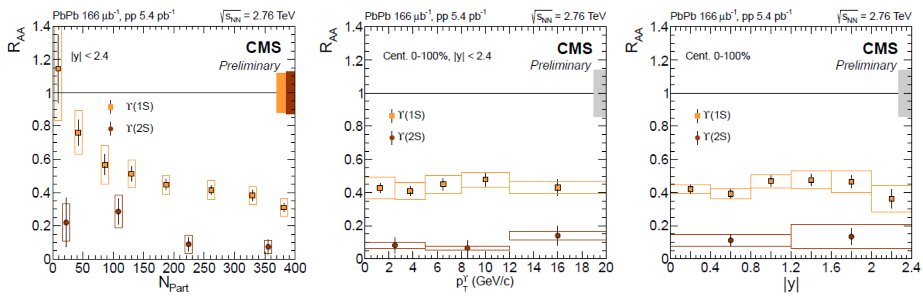

Fig. 10. Nuclear modification factor of $\Upsilon(1S)$ and $\Upsilon(2S)$ in PbPb collisions at 2.76 TeV [25]. Statistical and systematic uncertainties are displayed as error bars and boxes, respectively. Boxes at unity represent the global fully-correlated uncertainties. Left panel: R_{AA} as a function of centrality, given by the number of participating nucleons N_{part}. Middle panel: R_{AA} as a function of transverse momentum. Right panel: R_{AA} as a function of rapidity.

2.3. *Two-particle angular correlations*

Measurements for gold–gold collisions at the Relativistic Heavy Ion Collider (RHIC) have shown a long-range structure in the two-particle angular correlation functions, which has been attributed to the presence of the hot and dense matter formed in these collisions. The measurements were performed in terms of two-dimensional $\Delta\eta$–$\Delta\phi$ correlation functions, where $\Delta\eta$ is the difference in pseudorapidity and $\Delta\phi$ is the difference in azimuthal angle between the two particles. At the top RHIC energy of 200 GeV, the experiments have found the so-called "ridge" effect [26, 27], *i.e.* the long-range (large $\Delta\eta$) near-side ($\Delta\phi \approx 0$) two-particle correlations. A similar correlation structure has also been observed in 2.76 TeV PbPb collisions at the LHC [28, 29]. Unexpectedly, the effect appeared in very high-multiplicity pp collisions at 7 TeV as well [30]. It is present also in high-multiplicity (central) pPb collisions at 5.02 TeV [31–33].

While the ridge effect in nucleus–nucleus collisions is thought to arise from the response of a hydrodynamically expanding partonic medium to fluctuations of the initial collision geometry [34–36], various competing theoretical concepts have been proposed to explain the emergence of this phenomenon in *pp* and *p*Pb collisions. These include gluon saturation in the initial state of the collision (Color Glass Condensate) [37] but also hydrodynamic effects in the high-density systems possibly formed in the collisions at TeV energies [38, 39].

As the LHC accelerator started to deliver *pp* collisions at a new energy regime at $\sqrt{s} = 13\,\mathrm{TeV}$, there is a renewed interest in investigating the correlations, especially their energy dependence. The first measurement of long-range two-particle correlations for the LHC Run 2 *pp* data has been reported by the ATLAS Collaboration [40]. The CMS has also studied such correlations in *pp* collisions at 13 TeV [41]. The study was done as a function of track multiplicity[2] ($N_{\mathrm{trk}}^{\mathrm{offline}}$) and transverse momentum. The two-dimensional (2D) $\Delta\eta$–$\Delta\phi$ two-particle correlation functions for events with low and high multiplicities are shown in Fig. 11, for pairs of charged particles. For the low-multiplicity sample ($N_{\mathrm{trk}}^{\mathrm{offline}} < 35$), the dominant features are the correlation peak near $(\Delta\eta, \Delta\phi) = (0, 0)$, containing mostly pairs of particles originating from the same jet, and the structure elongated in $\Delta\eta$ at $\Delta\phi \approx \pi$, for pairs of particles from back-to-back jets. In high-multiplicity *pp* events ($N_{\mathrm{trk}}^{\mathrm{offline}} \geq 105$), in addition to the correlation structures related to jets, a "ridge"-like structure emerges at $\Delta\phi \approx 0$, extending over a range of at least 4 units in $|\Delta\eta|$.

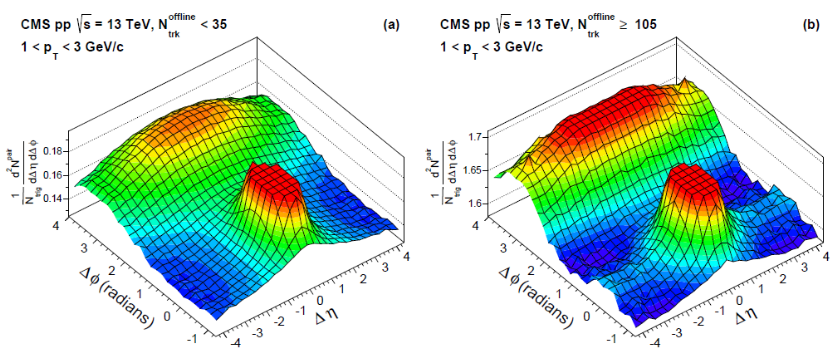

Fig. 11. The 2D $(\Delta\eta, \Delta\phi)$ two-particle correlation functions in *pp* collisions at 13 TeV for pairs of charged particles, both in the range of $1 < p_{\mathrm{T}} < 3\,\mathrm{GeV}/c$ [41]. Results are shown for (a) low-multiplicity events ($N_{\mathrm{trk}}^{\mathrm{offline}} < 35$) and for (b) high-multiplicity events ($N_{\mathrm{trk}}^{\mathrm{offline}} \geq 105$). The sharp peaks from jet correlations around $(\Delta\eta, \Delta\phi) = (0, 0)$ are truncated to better illustrate the long-range correlations.

[2] Track multiplicity, $N_{\mathrm{trk}}^{\mathrm{offline}}$, is defined as the number of charged particles reconstructed in the silicon tracker and having $|\eta| < 2.4$ and $p_{\mathrm{T}} > 0.4\,\mathrm{GeV}/c$.

The strength of long-range near-side correlations in pp collisions at 13 TeV was quantified and the yield associated with the ridge is shown in Fig. 12, where the energy and system size dependences are presented. The magnitude of the correlation exhibits a pronounced maximum in the range of $1 < p_{\mathrm{T}} < 2\,\mathrm{GeV}/c$ (panel (a) of Fig. 12) and an approximately linear increase with the charged particle multiplicity for $N_{\mathrm{trk}}^{\mathrm{offline}} > 40$ (Fig. 12 (b)). No collision energy dependence is visible as the overall correlation strength at $\sqrt{s} = 13\,\mathrm{TeV}$ is similar to that found in earlier pp data at $\sqrt{s} = 7\,\mathrm{TeV}$, but now it is measured up to much higher multiplicity values. Figure 12 (c) compares the associated yields in pp, pPb and PbPb collisions for $1 < p_{\mathrm{T}} < 2\,\mathrm{GeV}/c$ as a function of the track multiplicity. The comparison indicates a strong system size dependence.

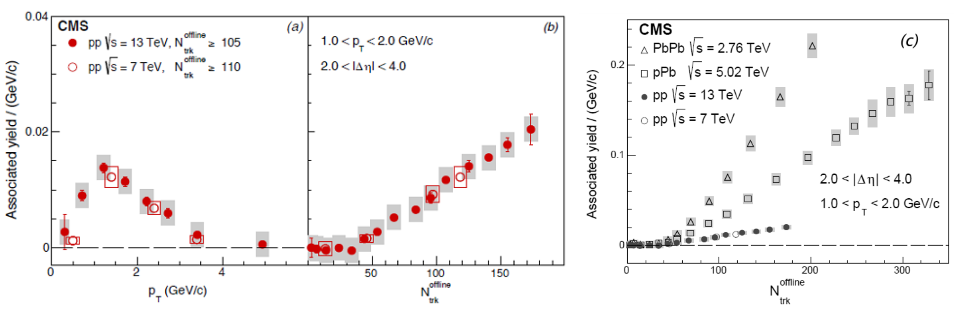

Fig. 12. Integrated associated yield for the near-side of the correlation function averaged over $2 < |\Delta\eta| < 4$ for pp data at $\sqrt{s} = 13\,\mathrm{TeV}$ (filled circles) and 7 TeV (open circles), pPb collisions at $\sqrt{s_{NN}} = 5.02\,\mathrm{TeV}$ (open squares), and PbPb collisions at $\sqrt{s_{NN}} = 2.76\,\mathrm{TeV}$ (open triangles) [41]. The error bars correspond to the statistical uncertainties, while the shaded areas and boxes denote the systematic uncertainties. Panel (a) shows the associated yield as a function of p_{T} for high multiplicity pp collisions. Panel (b) shows the associated yield as a function of multiplicity ($N_{\mathrm{trk}}^{\mathrm{offline}}$) for pp collisions. The p_{T} selection ($1 < p_{\mathrm{T}} < 2\,\mathrm{GeV}/c$) applies to both particles in each pair. Panel (c) shows the associated yield as a function of multiplicity for pp, pPb and PbPb collisions.

The CMS has observed the ridge effect also in two-particle angular correlations of an identified strange hadron (K_{S}^{0} or $\Lambda/\bar{\Lambda}$) and a charged particle ($h^{\pm}$) for high-multiplicity pPb collisions at 5.02 TeV, as shown in Fig. 13 [42]. In order to better understand these correlations, a Fourier decomposition of the 1D $\Delta\phi$-projected correlation functions for the long-range region ($|\Delta\eta| > 2$) has been performed. The second and third Fourier coefficients, called the elliptic (v_2) and triangular (v_3) flow respectively, were extracted. In hydrodynamic models, these coefficients reflect the created medium response to the initial collision geometry and its fluctuations.

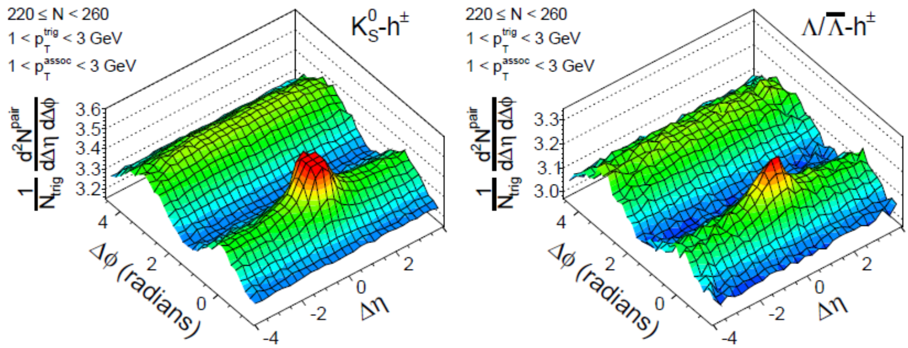

Fig. 13. The 2D $(\Delta\eta, \Delta\phi)$ two-particle correlation functions in pPb collisions at $\sqrt{s_{NN}} = 5.02$ TeV for pairs of a K^0_{S} or $\Lambda/\bar{\Lambda}$ trigger particle and a charged associated particle $(h^{\pm})$, with $1 < p_{\mathrm{T}}^{\mathrm{trig}} < 3$ GeV and $1 < p_{\mathrm{T}}^{\mathrm{assoc}} < 3$ GeV, in the multiplicity range of $220 \leq N_{\mathrm{trk}}^{\mathrm{offline}} < 260$ [42]. The sharp near-side peak from jet correlations is truncated to emphasize the structure outside that region.

Figure 14 (left) shows the v_2 values for K^0_{S} and $\Lambda/\bar{\Lambda}$ particles as a function of p_{T} for the high-multiplicity $(220 \leq N_{\mathrm{trk}}^{\mathrm{offline}} < 260)$ pPb data, along with the previously published results for charged particles [31]. In the low-p_{T} region ($p_{\mathrm{T}} < 2$ GeV$/c$), the v_2 values of K^0_{S} are larger than those for $\Lambda/\bar{\Lambda}$. Both of them are below the v_2 values of $h^{\pm}$ particles. As most charged particles are pions, the comparison indicates that lighter particle species exhibit a stronger azimuthal anisotropy signal. This mass ordering behavior is in agreement with the expectations of hydrodynamic models. A similar trend was first observed in nucleus–nucleus collisions at RHIC [43]. At higher p_{T}, the v_2 values of $\Lambda/\bar{\Lambda}$ are larger than those of K^0_{S}. The charged particle v_2 values fall between the values of the two identified strange hadron species.

The scaling behavior of v_2 divided by the number of constituent quarks, n_q, as a function of transverse kinetic energy[3] per quark, $\mathrm{KE_T}/n_q$, is presented in the middle row of Fig. 14. After scaling by n_q, the v_2 distributions of K^0_{S} and $\Lambda/\bar{\Lambda}$ are found to be in agreement. In nucleus–nucleus collisions, such a scaling is conjectured to be related to quark recombination [44, 45], which postulates that the collective flow is developed among constituent quarks before they combine into final-state hadrons. The particle species dependence of v_2 was also studied in PbPb collisions at 2.76 TeV, for the same multiplicity bin as for the pPb data, see Fig. 14 (right). Qualitatively, similar particle-species dependences of v_2 are observed. However, the mass ordering effect is found to be less evident in PbPb data than in pPb data.

[3] Transverse kinetic energy: $\mathrm{KE_T} \equiv \sqrt{m^2 + p_{\mathrm{T}}^2} - m$ accounts for the mass difference of particles.

In the hydrodynamic description, this may indicate that a stronger radial flow is developed in the central pPb collision as its energy density is higher than that for semi-peripheral PbPb data.

The triangular flow, v_3, of K^0_S and $\Lambda/\bar{\Lambda}$ particles was also extracted in pPb and PbPb collisions [42] (not shown here), and a similar particle species dependence of v_3 to that of v_2 was observed.

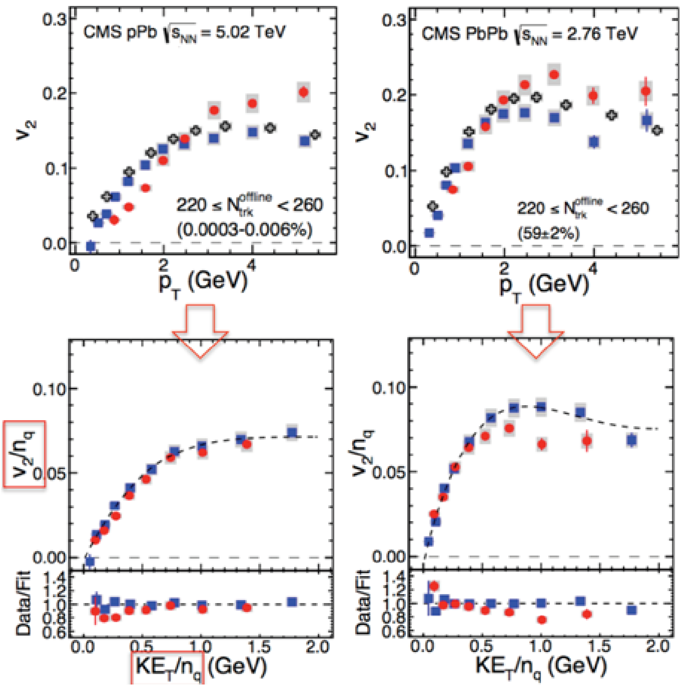

Fig. 14. Top row: v_2 results for K^0_S (filled squares), $\Lambda/\bar{\Lambda}$ (filled circles), and charged particles (open crosses) as a function of p_T for pPb collisions at $\sqrt{s_{NN}} = 5.02$ TeV (left panel) and PbPb collisions at $\sqrt{s_{NN}} = 2.76$ TeV (right panel), for the multiplicity range of $220 \le N_{\rm trk}^{\rm offline} < 260$ [42]. Middle row: $v_2/n_{\rm q}$ ratios for K^0_S and $\Lambda/\bar{\Lambda}$ particles as a function of $\mathrm{KE_T}/n_q$, along with a fit to the K^0_S results using a polynomial function. Bottom row: Ratios of v_2/n_q for K^0_S and $\Lambda/\bar{\Lambda}$ particles to the fitted polynomial function as a function of $\mathrm{KE_T}/n_q$. The error bars correspond to statistical uncertainties, while the shaded areas denote the systematic uncertainties.

3. Summary

The CMS heavy-ion program covers a wide range of physics observables studied in PbPb, pPb and pp collisions. In this paper, selected results on jet quenching, suppression of quarkonia and two-particle angular correlations have been presented, based on data from Run 1 of the LHC. All measurements give a consistent picture of QGP being formed in central PbPb collisions.

A strong parton energy loss in the medium created in PbPb collisions leads to jet quenching, which is the final-state effect as the phenomenon is not seen in pPb collisions. Due to jet quenching, fragmentation functions of jets in PbPb are modified, in comparison to the pp reference, and show an excess of particles at low p_{T}. The parton energy losses cause also emissions of low-p_{T} particles at large angles with respect to the quenched jet direction.

The measurements of R_{AA} for charmonium and bottomonium states in PbPb collisions confirm the suppression pattern expected from Debye screening in the hot, colored medium — the sequential melting of quarkonia. In addition, first detailed studies of Υ states have shown a strong centrality-dependent suppression and no dependence on rapidity and p_{T}.

The analyzes of two-particle angular correlations in PbPb, pPb and pp collisions at LHC energies resulted in the observation of the ridge effect in the three systems. A strong collision system size dependence of the ridge has been observed, with the strongest effect for PbPb collisions. The comparison of pp data at 7 TeV and 13 TeV (Run 2 data) points to no collision energy dependence.

At present, the data from Run 1 are still being analyzed, as well as newly gathered data of Run 2. Thus, more results are to come in the near future, making possible a deeper understanding of the rich phenomenology of the strongly interacting QCD matter.

This work was supported by the National Science Centre, Poland, grant 2014/14/M/ST2/00428.

REFERENCES

[1] S. Chatrchyan *et al.* [CMS Collaboration], *JINST* **3**, S08004 (2008).

[2] M.L. Miller *et al.*, *Annu. Rev. Nucl. Part. Sci.* **57**, 205 (2007).

[3] CMS Collaboration, CMS Public Heavy Ion Results,
`http://twiki.cern.ch/twiki/bin/view/CMSPublic/PhysicsResultsHIN`

[4] M. Gyulassy, M. Plumer, *Phys. Lett. B* **243**, 432 (1990).

[5] S. Chatrchyan *et al.* [CMS Collaboration], *Phys. Lett. B* **710**, 256 (2012).

[6] S. Chatrchyan *et al.* [CMS Collaboration], *J. High Energy Phys.* **1503**, 022 (2015).

[7] S. Chatrchyan *et al.* [CMS Collaboration], *Phys. Lett. B* **715**, 66 (2012).

[8] S. Chatrchyan *et al.* [CMS Collaboration], *Eur. Phys. J. C* **72**, 1945 (2012).

[9] CMS Collaboration, Physics Analysis Summary CMS-PAS-HIN-12-014 (2012), `http://cds.cern.ch/record/1472735`

[10] V. Khachatryan *et al.* [CMS Collaboration], *Eur. Phys. J. C* **75**, 237 (2015).

[11] CMS Collaboration, Physics Analysis Summary CMS-PAS-HIN-12-004 (2012), `http://cds.cern.ch/record/1472722`

[12] V. Khachatryan *et al.* [CMS Collaboration], `arXiv:1601.02001 [nucl-ex]`.

[13] S. Chatrchyan *et al.* [CMS Collaboration], *Phys. Rev. Lett.* **113**, 132301 (2014).

[14] V. Khachatryan *et al.* [CMS Collaboration], *Phys. Lett. B* **754**, 59 (2016).

[15] N. Armesto *et al.*, *Phys. Rev. D* **69**, 114003 (2004).

[16] S. Chatrchyan *et al.* [CMS Collaboration], *Phys. Rev. C* **84**, 024906 (2011).

[17] S. Chatrchyan *et al.* [CMS Collaboration], *Eur. Phys. J. C* **74**, 2951 (2014).

[18] V. Khachatryan *et al.* [CMS Collaboration], *J. High Energy Phys.* **1601**, 006 (2016).

[19] S. Chatrchyan *et al.* [CMS Collaboration], *Phys. Rev. C* **90**, 024908 (2014).

[20] CMS Collaboration, Physics Analysis Summary CMS-PAS-HIN-15-004 (2015), `http://cds.cern.ch/record/2030077`

[21] T. Matsui, H. Satz, *Phys. Lett. B* **178**, 416 (1986).

[22] S. Digal, P. Petreczky, H. Satz, *Phys. Rev. D* **64**, 094015 (2001).

[23] V. Khachatryan *et al.* [CMS Collaboration], *Phys. Rev. Lett.* **113**, 262301 (2014).

[24] S. Chatrchyan *et al.* [CMS Collaboration], *Phys. Rev. Lett.* **109**, 222301 (2012).

[25] CMS Collaboration, Physics Analysis Summary CMS-PAS-HIN-15-001 (2015), `http://cds.cern.ch/record/2030083`

[26] B. Abelev *et al.* [STAR Collaboration], *Phys. Rev. C* **80**, 064912 (2009).

[27] B. Alver *et al.* [PHOBOS Collaboration], *Phys. Rev. Lett.* **104**, 062301 (2010).

[28] S. Chatrchyan *et al.* [CMS Collaboration], *J. High Energy Phys.* **1107**, 076 (2011).

[29] S. Chatrchyan *et al.* [CMS Collaboration], *Eur. Phys. J. C* **72**, 2012 (2012).

[30] V. Khachatryan *et al.* [CMS Collaboration], *J. High Energy Phys.* **1009**, 091 (2010).

[31] S. Chatrchyan *et al.* [CMS Collaboration], *Phys. Lett. B* **724**, 213 (2013).

[32] B. Abelev *et al.* [ALICE Collaboration], *Phys. Lett. B* **719**, 29 (2013).

[33] G. Aad *et al.* [ATLAS Collaboration], *Phys. Rev. Lett.* **110**, 182302 (2013).

[34] B. Alver, G. Roland, *Phys. Rev. C* **81**, 054905 (2010).

[35] B. Schenke, S. Jeon, C. Gale, *Phys. Rev. Lett.* **106**, 042301 (2011).

[36] J. Xu, C.M. Ko, *Phys. Rev. C* **83**, 021903 (2011).

[37] K. Dusling, R. Venugopalan, *Phys. Rev. D* **87**, 094034 (2013).

[38] P. Bożek, *Phys. Rev. C* **85**, 014911 (2012).

[39] P. Bożek, W. Broniowski, *Phys. Lett. B* **718**, 1557 (2013).

[40] G. Aad *et al.* [ATLAS Collaboration], `arXiv:1509.04776 [hep-ex]`.

[41] CMS Collaboration, Physics Analysis Summary CMS-PAS-FSQ-15-002 (2015), `http://cds.cern.ch/record/2056346`

[42] V. Khachatryan *et al.* [CMS Collaboration], *Phys. Lett. B* **742**, 200 (2015).

[43] S.S. Adler *et al.* [PHENIX Collaboration], *Phys. Rev. Lett.* **91**, 182301 (2003).

[44] D. Molnar, S.A. Voloshin, *Phys. Rev. Lett.* **91**, 092301 (2003).

[45] R.J. Fries *et al.*, *Phys. Rev. Lett.* **90**, 202303 (2003).